Earth and Planetary Science Letters 578 (2022) 117325

Contents lists available at ScienceDirect

Earth and Planetary Science Letters

www.elsevier.com/locate/epsl

Crustal response to heavy rains in Southwest Japan 2017-2020

Kosuke Heki [a,*], Syachrul Arief [a,b]

[a] Department Natural History Sciences, Hokkaido University, Japan
[b] BIG, Bogor, Indonesia

ARTICLE INFO

Article history:
Received 19 May 2021
Received in revised form 19 November 2021
Accepted 26 November 2021
Available online 2 December 2021
Editor: J.-P. Avouac

Keywords:
heavy rain
GNSS
subsidence
hydrological model
Japan

ABSTRACT

Weather fronts stationary above Southwest Japan often bring disastrous heavy rains in early summer. Here we study four such episodes in each of four summers between 2017 and 2020, and investigate transient lithospheric subsidence caused by rainwater loads using the daily coordinates of a dense network of continuous GNSS stations. After applying a network filter to remove common mode errors, we isolated subsidence signals of 1-2 centimeters in flooded regions. Such subsidence recovered mostly in a day as rainwater drained rapidly to nearby ocean promoted by large topographic slopes. Spatiotemporal correlation between subsidence and precipitation was weak due possibly to rapid post-precipitation migration of rainwater. However, a strong correlation was found between subsidence and rain spatially integrated over the entire Southwest Japan, i.e., bulk subsidence of ~0.1 km^3 (equivalent to the uniform subsidence ~0.6 mm) occurred for every 1 Gt rainwater per day. This linearity breaks down for rains exceeding ~10 Gt/day as rainwater possibly exceeds the water-holding capacity of forest catchments.

1. Introduction

Disastrous heavy rains occur in Southwest Japan almost every summer when stationary weather fronts (Bai-u front) extend WSW-ENE from East China Sea to the Japanese Islands. Vast amounts of water vapor from ocean transported eastward along such fronts generate a cluster of cumulonimbus clouds, thereby causing torrential downpours along linear rainbands. Recent global warming may have enhanced the probability of their occurrence (Imada et al., 2020). In fact, disastrous rain episodes in Southwest Japan have recurred every summer since 2017. The 2017 and 2019 rains were relatively local, and damages concentrated on northern Kyushu. However, those in 2018 and 2020 spread over the entire Southwest Japan (and partly Northeast Japan).

In Japan, a dense network of continuous receiving stations of global navigation satellite system (GNSS), known as GEONET (GNSS Earth Observation Network), is run by Geospatial Information Authority of Japan (GSI) (Tsuji and Hatanaka, 2018). Dense GNSS networks have been used to study heavy rains in two different ways, i.e., as a sensor of water vapor and of transient crustal movements due to rainwater load. For the former, Arief and Heki (2020) used GEONET data to analyze the water vapor dynamics during the heavy rain episodes in Southwest Japan 2017-2019. For the latter, Milliner et al. (2018) studied crustal deformation in southern North America in response to Hurricane Harvey stormwater in 2017. Zhan et al. (2021) first studied both the water vapor and crustal subsidence produced by super typhoon Hagibis, which drenched Northeast Japan in October 2019.

Such heavy rain episodes brought by stationary weather fronts often continue for a week or more, in contrast to a typhoon passage lasting for only a day or two. This enables us to investigate the correlation between precipitation and subsidence using various approaches. First, we select a certain GNSS station and a nearby rain gauge and examine correlation between the two quantities over a long period (single-site, long-period approach). Secondly, we select the day with the largest rainfall and study their correlation over the whole Southwest Japan (multi-sites, single-day approach). In both approaches, the rain and subsidence are expected to show positive correlations. At the same time, we anticipate that high mobility of rainwater immediately after precipitation may blur such correlations. Third, we compare rain and subsidence integrated over the whole Southwest Japan, quantities less affected by post-precipitation water migration. We will then explore the balance between precipitation and runoff to understand how rainwater is stored on land and depresses the lithosphere in Southwest Japan.

2. Rain and subsidence data

For the precipitation data, we use hourly rain gauge data from the dense meteorological sensor network AMeDAS (Automatic Meteorological Data Acquisition System) run by Japan Meteorological

* Corresponding author.
E-mail address: heki@sci.hokudai.ac.jp (K. Heki).

https://doi.org/10.1016/j.epsl.2021.117325

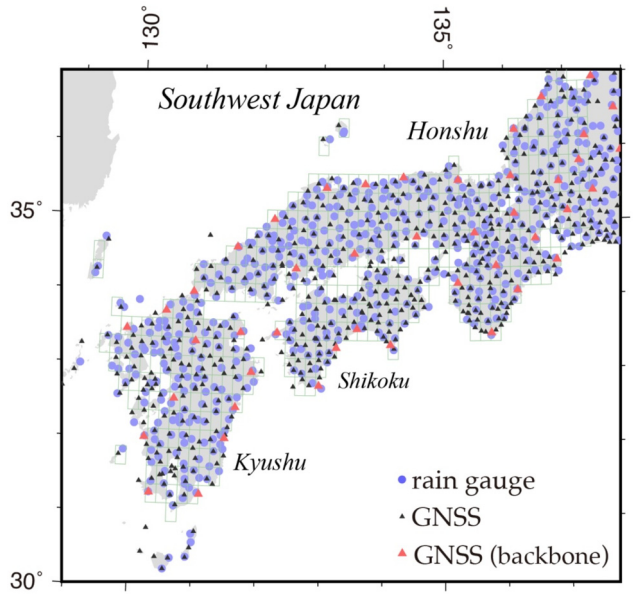

Fig. 1. Distribution of AMeDAS rain gauges (blue circles) and GEONET GNSS stations (black triangles). Red triangles indicate backbone GNSS stations used to remove common mode errors. ~400 small rectangles in green cover the whole Southwest Japan and are used in calculating the total amount of rain and subsidence of the entire region. (For interpretation of the colors in the figure(s), the reader is referred to the web version of this article.)

Agency (JMA), with density comparable to GEONET (Fig. 1). In order to calculate total amount of rain over Southwest Japan, we cover the whole region with rectangles shown in Fig. 1 and calculated average precipitations within individual rectangles (interpolated from adjacent rectangles when no rain gauges are available). Then, we sum the products of the rain and the rectangle areas to derive the total volume of rain (1 Gigaton is 1 cubic kilometers of water). Fig. 2d shows the hourly precipitation over Southwest Japan during the 2018 heavy rain episode. Heavy rains brought by stationary weather fronts often continue for a week or more, in contrast to the precipitation by the 2019 typhoon Hagibis lasting just a day (Zhan et al., 2021).

In 2021, the final solution of the GEONET daily coordinates, known as the F3 solution (Nakagawa et al., 2009), is replaced with the F5 solutions. This new solution is obtained with the data from Global Positioning System (GPS) satellites using the Bernese software package (Takamatsu et al., 2020). Treatment of atmospheric delays was updated to improve the vertical position accuracy. They employed the VMF1 atmospheric mapping function (Böhm et al., 2006) and increased the temporal resolution of tropospheric delay/gradient to 1-hour/3-hour (it was 3-hour/24-hour in F3). The station coordinates are linked to the IGb14 reference frame through ~100 stations distributed worldwide.

We correct for the common mode errors in the F5 solution following Zhan et al. (2021). We first select ~100 "backbone" stations (first generation GEONET stations) evenly distributed in Japan and defined the median coordinates over a 31-days period including the heavy rain episode as the "reference coordinates". The backbone stations are partly shown in Fig. 1 and the whole network can be seen in Fig. S1b. For each of the 31 days, we estimate the 7 parameters of the Helmert transformation (3 translations, 3 rotations, 1 scale) to minimize the difference between the observed and reference coordinates of the backbone stations. Then, we apply the daily transformation parameters to adjust the observed coordinates of all the GEONET stations. We neglect tectonic movements of the stations within the 31-days period. A test shown in Fig. S1 confirms that this procedure does not reduce the water signals, the target of this study. In this test, we excluded ~10% of stations, located within the heavy rain region, from the backbone stations and confirmed this exclusion did not cause significant changes in the vertical displacement time series. In fact, the center of heavy rainfall moves day by day, and the subsidence area also moves around within Southwest Japan as seen in Fig. S2.

Fig. 2 shows the vertical position time series of six stations in Shimane, western Honshu, over a 31-days period encompassing the 2018 heavy rain episode, relative to the median during this period. Improvement of repeatability from F5 to F5 with common error removed (F5C) reflects the reduction of such errors. The average vertical position shows clear subsidence on 2018 July 6, when the rainfall was the most intensive in Southwest Japan (see next Section). Fig. S3 shows the time series of atmospheric pressure at sea level during the 2018/2020 heavy rain episodes. Unlike typhoon passages, atmospheric pressure changed little, and vertical movements caused by atmospheric load changes would have been small. Here, we did not apply atmospheric load corrections to the vertical movements. Zhan et al. (2021) compared such F5C solution with the coordinates made available by University of Nevada Reno (UNR) (Blewitt et al., 2018). They did not show systematic differences but had random differences of up to ~5 mm. Fig. S4 compares the F5C daily solution of two GEONET stations with those by the kinematic solution (5 minutes interval) downloaded from UNR. An analysis of kinematic solutions is beyond the scope of the current study but could be considered in the future.

The average positions of the six stations (bottom, Figs. 2) show much less scatter than those of the individual stations. This suggests that spatial averaging is effective at reducing random errors. In this study, we perform such spatial averaging using a Gaussian filter with averaging radius of 20 km (Wahr et al., 1998) (Fig. S5). An example of horizontal displacements on the day of tremendous rainfall is shown in Fig. S5b. Horizontal displacements reflect azimuthal asymmetry of loads around stations. They are much influenced by patchy distribution of rainwater loads due to short wavelength topography of the studied area. We consider it difficult to extract useful information from horizontal components, and only vertical components are used in this study.

3. Correlation between rain and subsidence

3.1. GNSS site 0688 in northern Kyushu

First, we compare rain and subsidence at a single site, i.e., a pair of rain gauge (Asakura) and nearby GNSS station (0688) (Fig. 3a). They are in northern Kyushu, the region affected by all the four heavy rain episodes 2017-2020. We extract 31-day periods in summer from 2017-2020 that include heavy rain episodes and compare hourly rain and the F5C daily subsidence in Fig. 3d. The two quantities are positively correlated (Fig. 3b) but not simply linear. Subsidence of ~1 cm or more often occurs when rain rates reach tens of mm per hour. However, the largest hourly rain on 2017 July 5 was not associated with large subsidence. In fact, the 2017 heavy rain was quite local (Fig. S6a) and covered only a part of northern Kyushu. We suspect that the high mobility of rainwater made the correlation weak, i.e., the behavior of site 0688 may reflect precipitation over a larger area surrounding the station. Indeed, we replaced the rain data from a single rain gauge with the average of 13 rain gauges near the 0688 station (Fig. 3e), and this slightly increased the correlation (Fig. 3c). We tried several other pairs of GNSS stations and nearby rain gauges, but none of the results showed strong correlations.

3.2. Heavy July rains

The 2018 and 2020 heavy rains continued over a week in early July. In Fig. 4a-d, we select 5 days (July 3-7) and compare distributions of precipitation and subsidence. We show the daily rain

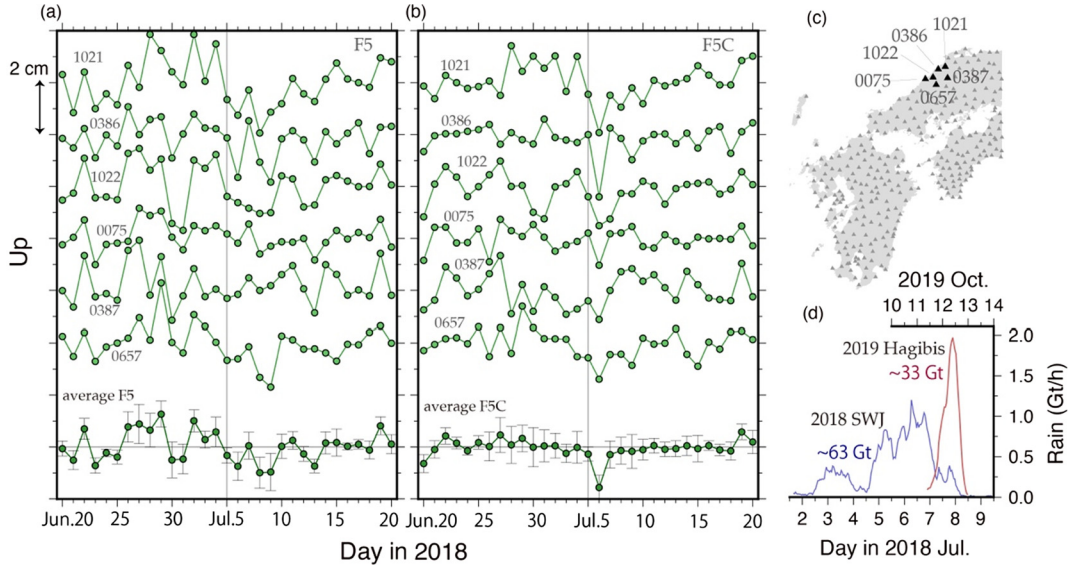

Fig. 2. Vertical position time series at 6 GNSS stations in western Honshu (see (c) for positions) by raw F5 solutions (a) and F5 corrected for common mode errors (F5C) (b) over ±15 days period around July 5, 2018. At the bottom we show their averages (dark green). Error bars of the average positions indicate the standard deviation of the six stations. Irregular fluctuations in the raw F5 time series largely disappear by removing the common mode errors leaving true subsidence on July 6. (d) compares hourly rains on land in the 2018 Southwest Japan heavy rain (~63 Gt in total) with those during the passage of the 2019 typhoon Hagibis (~33 Gt in total) (Zhan et al., 2021).

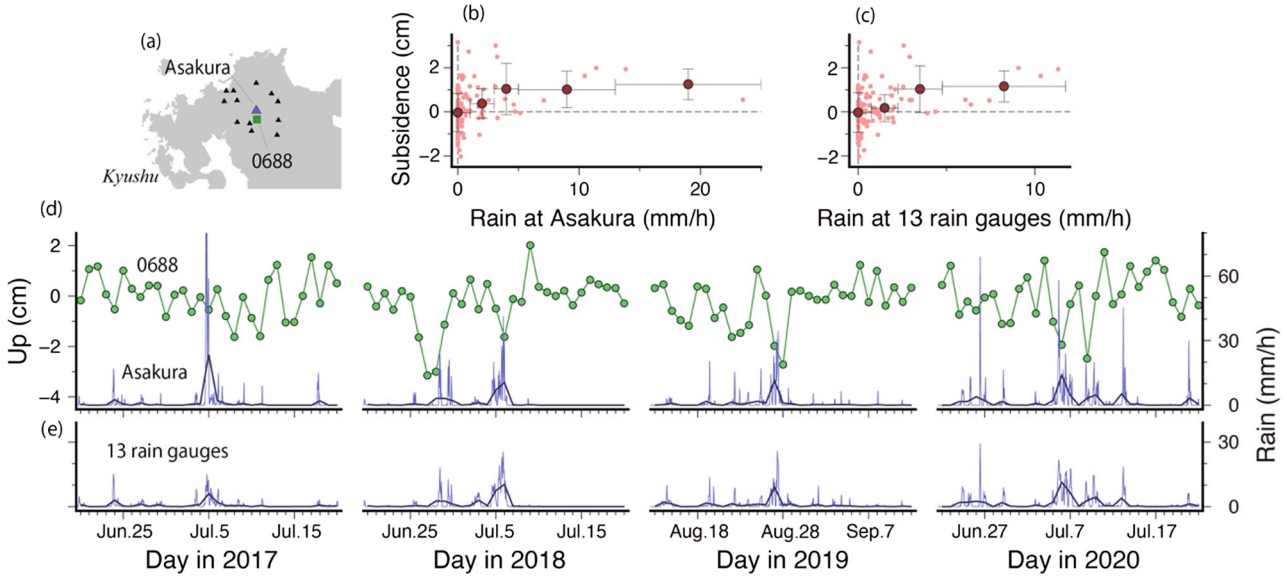

Fig. 3. The 0688 GNSS station in northern Kyushu and a nearby rain gauge at Asakura (large triangle), and 12 rain gauges within ~50 km from Asakura (small triangles) (a). The time series of vertical position (F5C solution, green circles) and hourly rain (light blue) and daily average hourly rain (dark blue) are shown in (d). The rain at Asakura and subsidence of site 0688 show only weak correlation (correlation coefficient: 0.302) (b). The correlation slightly increases (correlation coefficient: 0.376) (c) by replacing the rain at Asakura with the average rain at 13 rain gauges (including Asakura) (e). Dark red circles and error bars in (b, c) indicate average vertical displacements and standard deviations for 4-5 different ranges of the average rain.

calculated from 0:00 UT to 24:00 UT and the total amounts of rainfall onto the Southwest Japan land area are given at the right bottom corner of the panels in Gt. According to these values, the amount of rainfall exceeded 10 Gt on two days, July 5 and 6 in 2018, and three days, July 3, 6, and 7 in 2020. The largest daily rain of 21.7 Gt was recorded on July 6, 2018. A high-resolution precipitation distribution is available from radar rain gauge analyzed precipitation (RRAP) data by JMA, and Fig. S7 shows examples for the 2018 heavy rain episode. We confirmed that total amounts of daily rains from the AMeDAS rain gauges are consistent with the RRAP data within a few percent.

In Fig. 4b, d, we show spatial distribution of subsidence measured with GNSS on the same days. We did spatial averaging using a Gaussian filter with averaging radius of 20 km (Fig. S5). Subsidence occurs over large areas especially on the five extremely rainy days (July 5,6, 2018 and July 3, 5 and 6, 2020). We select 2018 July 6 (the day of maximum precipitation) and show correlation between the 24-hour rain on that day and subsidence at the rain gauge stations interpolated from GNSS data in Fig. 4e. The correlation between the two quantities (correlation coefficient is 0.453) is statistically significant (see e.g., https://www.real-statistics.com/statistics-tables/pearsons-correlation-table/), but the large dispersion of data suggests they are not simply proportional.

Like in the single-site long-period case, the weak correlation could be largely due to post-precipitation water redistribution. For example, the runoff of water downstream would cause the region experiencing subsidence to shift downstream with time as seen in the different spatial distribution of precipitation (Fig. 4a,c) and

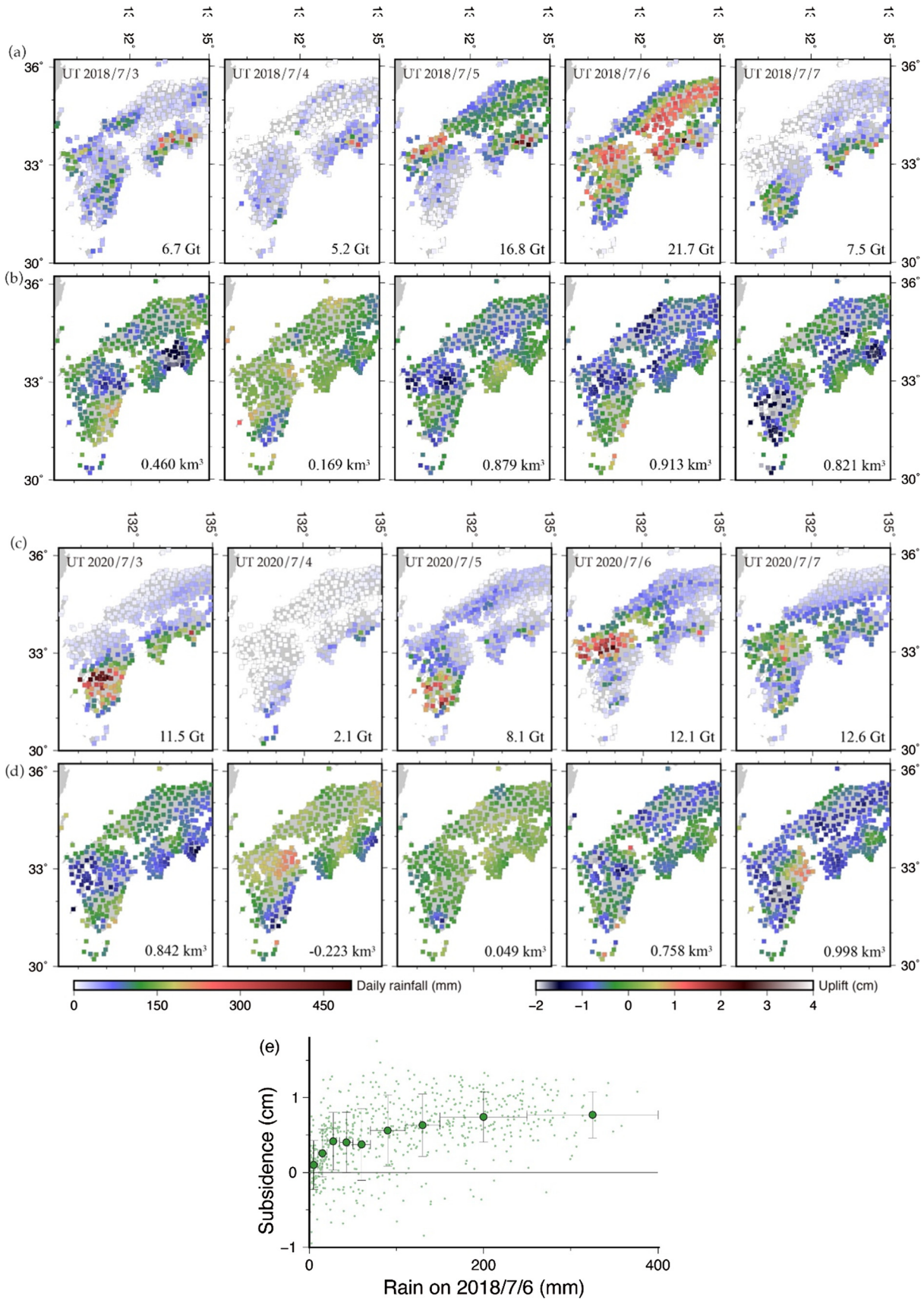

Fig. 4. (a) Distributions of daily precipitation in Southwest Japan July 3-7, 2018, calculated by integrating hourly rainfall over period 0:00-24:00 in UT. (b) Vertical position of GNSS stations in Southwest Japan after spatial smoothing using a Gaussian filter with averaging radius of 20 km. (c) and (d) show period July 3-7, 2020. (e) Correlation between the amount of rain at rain gauge stations on 2018 July 6 (horizontal axis) and the subsidence on the same day there (interpolated from GNSS stations). We divided the rain into 9 ranges and showed average vertical displacements and standard deviations with dark green circles and error bars.

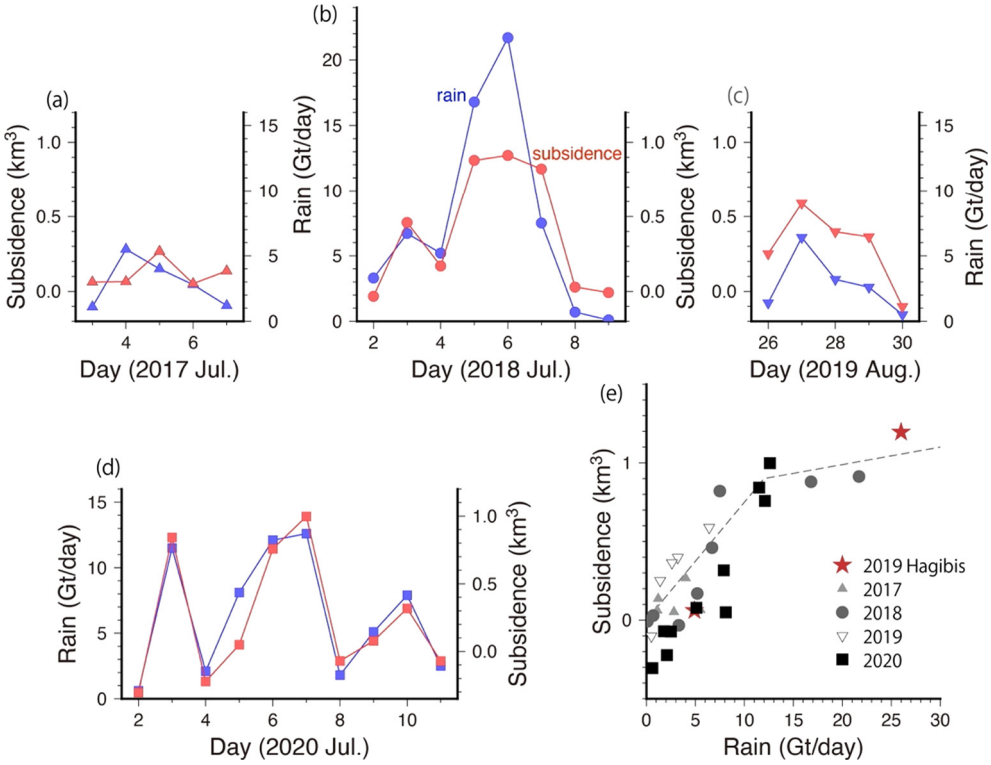

Fig. 5. Comparison between volumetric subsidence (red) and daily total rainwater mass (blue) for 5-, 8-, 5- and 10-days periods covering 2017 (a), 2018 (b), 2019(c), and 2020 (d) heavy rain episodes, respectively. They show strong positive correlation, although subsidence seems to saturate on days with total rain exceeding ~10 Gt (b). (e) shows the relationship between the daily rainwater and volumetric subsidence for all the days shown in (a-d), and the case of the 2019 typhoon Hagibis reported in Zhan et al. (2021). They show linear relationship with a possible change in slope around 10 Gt/day.

subsidence (Fig. 4b,d). A good example is given in Fig. 2, where six stations near the north coast of western Honshu show large subsidence on July 6, 2018. Such subsidence is larger than that in the backbone range where it rained more (Fig. 4a,b). This reflects the transportation of rainwater from the mountains down along the Gonokawa river, which exhibited large water level enhancement on that day. The river water level and the map are given in Fig. S8.

3.3. Spatially integrated subsidence

Next, we compare subsidence and precipitation over the whole Southwest Japan. Such quantities are less influenced by water transportation and expected to be strongly correlated. As seen in Fig. 4, subsidence occurs over large areas on the five extremely rainy days (July 5,6, 2018, and July 3, 5 and 6, 2020). On the other hand, subsidence is not remarkable on the days of small amount of rain such as July 4, both in 2018 and 2020. Here we define a new integrated quantity. We multiply the average subsidence in individual blocks by the area of each block (blocks shown as green boxes in Fig. 1). If blocks do not include GEONET stations, we interpolate subsidence from surrounding blocks. We then sum the results from all blocks together to arrive at an estimate of "volumetric subsidence". We expect such volumetric subsidence scales linearly with the total rainwater storage in Southwest Japan. The volumetric subsidence in km^3 is given at the bottom right corner of panels in Fig. 4b, d (negative values indicate dominance of uplift). Because the total area studied here is $\sim 1.7 \times 10^5$ km^2, 1 km^3 volumetric subsidence corresponds to the average subsidence of ~5.9 mm. On the days with rains exceeding 10 Gt, volumetric subsidence is nearly 1 km^3.

Fig. 5a-d compares the two quantities, volumetric subsidence and total rain mass, over the period of 5, 8, 5 and 10 days covering the heavy rain episodes in 2017, 2018, 2019, and 2020. Spatial distributions of rain and subsidence for the 2017 and 2019 episodes are given in Fig. S6. The two curves show striking similarity, i.e., the two quantities are nearly proportional. At the same time, subsidence does not catch up with the rain on July 5, 6, 2018, suggesting that the proportionality may break down on days of extreme rains due possibly to rapid runoff into the ocean.

Fig. 5e compares the two quantities for all the episodes. It includes two days of heavy rains caused by the 2019 typhoon Hagibis reported in Zhan et al. (2021), where uplifts caused by negative atmospheric loads are already corrected using the Green's function by Farrell (1972) (we did not correct other data for atmosphere). This typhoon brought rains mainly in eastern Honshu over an area comparable to the 2018/2020 heavy rains in Southwest Japan. The typhoon data seem to align on the same trend as the heavy rains in Southwest Japan. It is also recognized that the points for the 2020 case are systematically shifted downward by ~0.2 km^3. This might arise from the wrong assumption of reference positions. Expanding the period to calculate the medians from ±15 to ±30 days did not make significant changes.

4. Discussion

4.1. Problems in the inversion for water distribution

With the crustal subsidence data given in Fig. 4b, d, we could estimate surface water distribution using the Green's function as done in Milliner et al. (2018). In Japan, however, this results in serious overestimation of the water amount (Zhan et al., 2021). The GEONET stations in Japan are installed in concave terrains, e.g., along valleys and within basins. By comparing the sensitivity of subsidence to precipitation between stations located in flat lands and highly concave terrains, Zhan et al. (2021) demonstrated that subsidence signals in the latter are biased high due mainly to (1) water concentration around GNSS stations, and partly to (2) lower rigidity in shallow sediment layers beneath GNSS stations

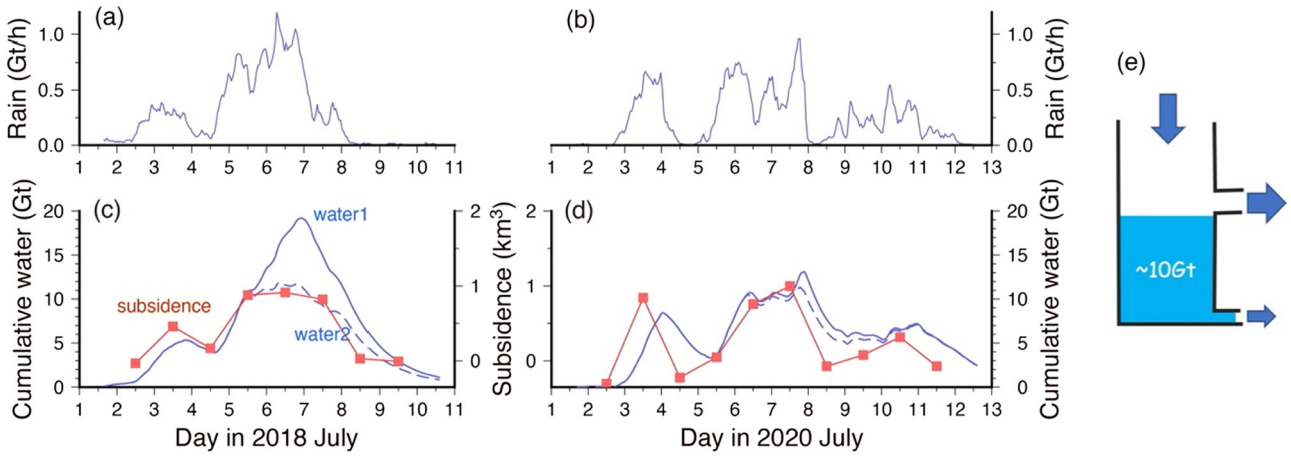

Fig. 6. Hourly rain over the entire Southwest Japan for the 2018 (a) and 2020 (b) heavy rain episodes. We calculated the cumulative rain assuming that 4% of the total storage drained in an hour (similar to exponential decay with a time constant ~24 hours) (blue curve labeled as water 1). We also assumed that this ratio changes to 30% for water exceeding 10 Gt (broken curve labeled as water 2), for the 2018 (c) and 2020 (d) cases. This can be modeled by a tank having two spigots with the upper one working for water beyond ~10 Gt (e).

than global average. Fig. S9 indicates that this topographic problem is also significant in Southwest Japan. In this study, we just show one example of inversion for surface water load using the data on 2018 July 6 to confirm the existence of this problem (Fig. S10). The total amount of the estimated water (~61 Gt) is more than twice as large as the precipitation on that day. Comparison of total precipitation inferred from radar (Fig. S7) and rain gauge (Fig. 4a) suggests that their errors do not exceed a few percent and are not responsible for this large inconsistency.

Here we do not pursue this problem further. Instead, we focus on the empirical relationship between crustal subsidence and precipitation in Southwest Japan and how we can explain the temporal evolution of precipitation and subsidence with a simple hydrological model. It should be noted that the volumetric subsidence in Southwest Japan derived in this study is overestimated (larger than the true volume of crustal subsidence) mainly due to the topographic problem. Hence, the ratio of volumetric subsidence to precipitation needs to be modified in regions with different topographic characteristics. For example, the overestimation problem would not occur in flat continental regions. The ratio will also depend on how the GNSS stations are deployed. If they are installed at high elevation, e.g., hilltops, subsidence signals would be biased low.

4.2. A simple hydrological model

Changes in total water storage (dS) are often modeled with three fluxes, precipitation (input, P), evapotranspiration (output, E), and runoff (output, Q), i.e., $dS = P - E - Q$. According to Palmer and Havens (1958), potential monthly evapotranspiration in July in the studied area is ~16 cm (~5 mm/day, equivalent to ~0.035 Gt/h for the entire Southwest Japan). We neglect it in the present discussions because of its relative insignificance and assume only precipitation and runoff. Then we model the behavior of water on Southwest Japan using a tank with input (rain) and output (runoff) (Fig. 6e). If the flux through the drain is proportional to the total water storage, the water storage would balance at a level proportional to the input flux, i.e., rain rate. This explains the behavior shown in Fig. 5, where volumetric subsidence values are roughly proportional to daily rains.

Fig. 6a, b shows hourly rain spatially integrated over the whole Southwest Japan. We simulate hourly water storage changes using the water-balance model above over periods of 10 days (2018) and 12 days (2020) assuming that 4% of the total storage is lost in one hour, output through the lower spigot of the tank (Fig. 6e). This corresponds to an exponential decay of rain with a time constant of ~24 hours. Decays in such time constants are often found in the river water levels as shown in Fig. S11. We assumed water storage is zero at the beginning of the simulation. The calculated total water storage changes are shown as blue solid curves labeled "water 1" in Fig. 6c, d. These curves were derived only from precipitation and hydrological modeling, and not from the GNSS data.

We assume that the lower spigot works for water up to ~10 Gt. To realize the saturation of water storage beyond this critical amount, we assumed that the decay ratio increases from 4% to 30% for the amounts exceeding 10 Gt. This corresponds to the activation of the upper (and more efficient) spigot in Fig. 6e, effective only beyond this critical level. The revised curves for the water storage, given with broken curves as "water 2", better approximate the behavior of volumetric subsidence in 2018 in Fig. 6c. The increased decay ratio (30%) is not well constrained in this study, i.e., any ratios exceeding ~20% give reasonable fits in Fig. 6c. Volumetric subsidence is ~1 km^3 for water storage of 10 Gt. As stated in the previous section, this coefficient (~0.1 km^3/Gt) is valid in Japan but needs to be revised for regions with different situations, e.g., terrain concavity around the GNSS stations, and possibly permeability and porosity of soils and bedrock.

Here we speculate on the physical entities of the two spigots in Fig. 6e. The lower spigot would correspond to discharge through normal river channels bounded by levees. The upper spigot could represent water flow beyond the river levees after they are partly washed out. In fact, damages to river levees are reported at 35 points during the 2018 July heavy rain and at 140 points during the passage of the typhoon Hagibis in 2019 according to the Ministry of Land, Infrastructure, Transport and Tourism, Japan (www.mlit.go.jp/en/index.html). On the other hand, only 5 or less damages were reported during the 2017, 2019, and 2020 heavy rains when daily rains did not far exceed 10 Gt.

Another, perhaps more plausible, explanation would be related to the water capacity of typical forests in Japanese mountain areas. Water-holding capacity, defined as the product of porosity by soil depth, is estimated as the basin storage by analyzing the relationship between rainfall and abstraction (loss of runoff due to water held within forest). Fujieda (2007) compiled data from 52 forest catchments in Japan and found the basin storage ranges from 50 to 250 mm depending on surface geology and soil type. In our study, 10 Gt water over the whole Southwest Japan corresponds to ~60 mm average thickness, and such thickness will be two- or

threefold within the heavy rain areas. Hence, the critical amount of rain may reflect the water saturation within forest catchments, i.e., rainwater exceeding this capacity would directly flow into rivers without being retained temporarily within forests. This may also explain the activation of the higher spigot for rains exceeding 10 Gt in a day.

We presented a simple hydrological model, and it would not be a unique one to explain the behavior. Nevertheless, it gives us an insight into the essential behavior of a mountainous island as a water tank. Rainwater dynamics revealed in this study would be different in flat continental areas like the southern USA (Milliner et al., 2018) and in a continental area with long-wavelength basins and mountain ranges like California (Argus et al., 2017). However, lithosphere in mountainous and rainy islands, like the Philippines, Taiwan, and Indonesia, are expected to respond to heavy rains in a similar manner to Japan.

CRediT authorship contribution statement

KH designed the study, analyzed and interpreted the data, and wrote the draft article. SA performed data analysis in an early stage of the study. Both agreed on the final version of the manuscript.

Declaration of competing interest

The authors declare that they have no known competing financial interests or personal relationships that could have appeared to influence the work reported in this paper.

Acknowledgements

We downloaded the F5 solution of the GEONET daily coordinates from the ftp server of GSI terras.gsi.go.jp. Rain gauge data and radar rain gauge analyzed precipitation data are available from JMA at www.jma.go.jp. The river water level data are available from www.river.go.jp/e/. We thank Donald Argus (JPL) and Hilary Martens (Univ. Montana) for constructive and thoughtful comments.

Appendix A. Supplementary material

Supplementary material related to this article can be found online at https://doi.org/10.1016/j.epsl.2021.117325.

References

Argus, D.F., Landerer, F.W., Wiese, D.N., Martens, H.R., Fu, Y., Famiglietti, J.S., Thomas, B.F., Farr, T.G., Moore, A.W., Watkins, M.M., 2017. Sustained water loss in California's mountain ranges during severe drought from 2012 to 2015 inferred from GPS. J. Geophys. Res., Solid Earth 122, 10,559–10,585.

Arief, S., Heki, K., 2020. GNSS meteorology for disastrous rainfalls in 2017–2019 summer in Southwest Japan: a new approach utilizing atmospheric delay gradients. Front. Earth Sci. 8, 182.

Blewitt, G., Hammond, W.C., Kreemer, C., 2018. Harnessing the GPS data explosion for interdisciplinary science. Eos 99, 1–2.

Böhm, J., Werl, B., Schuh, H., 2006. Troposphere mapping functions for GPS and very long baseline interferometry from European Centre for Medium-Range Weather Forecasts operational analysis data. J. Geophys. Res., Solid Earth 111, B02406.

Farrell, W.E., 1972. Deformation of the Earth by surface loads. Rev. Geophys. Space Phys. 10 (3), 761–797.

Fujieda, M., 2007. Water-holding capacity and basin storage at forest catchments in Japan. Bull. Forestry Forest Products Res. Inst. 6, 101–110 (in Japanese with English abstract).

Imada, Y., Kawase, H., Watanabe, M., Arai, M., Shiogama, H., Takayabu, I., 2020. Advanced risk-based event attribution for heavy regional rainfall events. npj Clim. Atmos. Sci. 3, 37.

Milliner, C., Materna, K., Bürgmann, R., Fu, Y., Moore, A.W., Bekaert, D., Adhikari, S., Argus, D.F., 2018. Tracking the weight of Hurricane Harvey's stormwater using GPS data. Sci. Adv. 4 (9), eaau2477.

Nakagawa, H., Toyofuku, T., Kotani, K., Miyahara, B., Iwashita, C., Kawamoto, S., Hatanaka, Y., Munekane, H., Ishimoto, M., Yutsudo, T., Ishikura, N., Sugawara, Y., 2009. Development and validation of GEONET new analysis strategy (version 4). J. Geogr. Surv. Inst. 118, 1–8 (in Japanese).

Palmer, W.C., Havens, A.V., 1958. A graphical technique for determining evapotranspiration by the Thornthwaite method. Mon. Weather Rev. 86, 123–128.

Takamatsu, N., Muramatsu, H., Furuya, T., Abe, S., Hiyama, Y., 2020. The development of the new analysis strategy of GEONET. paper presented at In: The 2020 Fall Meeting of American Geophys. Union. Dec. 10.

Tsuji, H., Hatanaka, Y., 2018. GEONET as infrastructure for disaster mitigation. J. Disaster Res. 13 (3), 424–432.

Wahr, J., Molenaar, M., Bryan, F., 1998. Time variability of the Earth's gravity field: hydrological and oceanic effects and their possible detection using GRACE. J. Geophys. Res. 103, 30205–30229.

Zhan, W., Heki, K., Arief, S., Yoshida, M., 2021. Topographic amplification of crustal subsidence by the rainwater load of the 2019 typhoon Hagibis in Japan. J. Geophys. Res., Solid Earth 126, e2021JB021845.